MSDE

PAPER

View Article Online
View Journal | View Issue

Cite this: *Mol. Syst. Des. Eng.*, 2024, **9**, 947

Green synthesis of a thermo/photochromic doped cellulose polymer: a biocompatible film for potential application in cold chain visual tracking†

A. Azzali ‡§ M. F. Di Filippo,§ L. Bertuccioli, S. Lilburn,¶ S. Panzavolta, * F. Grepioni and S. d'Agostino *

To mitigate food losses and ensure a robust cold chain in transportation, sensors play a pivotal role in swiftly and visibly monitoring storage conditions. The most commonly used indicators for reporting temperature violations are based on devices capable of signaling when a threshold temperature has been reached or exceeded or on disposable colorimetric sensors. A potential alternative, which uses reusable colorimetric sensors, may come from utilizing systems capable of displaying reversible color changes upon temperature variations; in this regard, molecules exhibiting thermo- and photochromic properties such as *N*-salicylideneaniline derivatives (anils) have emerged as promising candidates due to the simplicity of their synthesis and their ability to respond to temperature and light stimuli. In this study we have synthesized a family of anils through mechanochemistry, focusing on H/F substituents on the bromoaniline residue. The compounds were fully characterized using XRD and thermal techniques, and their thermo- and photochromic properties were explored *via* infrared spectroscopy. Among the series, the most suitable compound, *i.e.*, a photochromic one showing a neat color change (from white to red/orange) quickly naked eye-detectable and whose back reaction is slow or virtually negligible at low temperatures, was identified and incorporated into a carboxymethyl cellulose (CMC) biopolymer matrix to produce a composite film, which was further characterized *via* XRD, thermal analyses and mechanical tests. The selected compound maintained its photochromic behavior upon embedding, and UV irradiation induced a color change in the film from colorless to red, while reversibility was evaluated at different temperatures (−19 °C, 4 °C and RT) using UV-vis spectroscopy. The composite film maintained a deep red color at −19 °C and 4 °C for seven weeks, while rapidly reversing to white/yellowish at room temperature, making it a suitable candidate for the development of sensors for cold chain transport and scenarios requiring rapid visual inspection of storage conditions.

Received 25th March 2024,
Accepted 30th May 2024

DOI: 10.1039/d4me00055b

rsc.li/molecular-engineering

Design, System, Application

Cold chain trackers are systems designed to monitor and track perishable goods' temperature and environmental conditions throughout the supply chain, from production to distribution and storage. Nowadays, most trackers are divided into devices and colorimetric indicators for visual inspection. Designing novel cold chain trackers with visual inspection capabilities is paramount. These trackers allow real-time feedback on the condition of goods, enabling quick identification of potential issues. In this work, we used molecular design to synthesize a family of crystalline thermo- and photo-chromic pigments and the possibility of incorporating them within a biodegradable GRAS biopolymer matrix to create tags of the composite material to be used as indicators. Tests at various storage temperatures were also performed. We believe that this work can potentially contribute to developing novel cold-chain trackers for visual inspection working on a broader range of temperatures.

1. Introduction

Food waste can be defined as the collection of products discarded from the agri-food chain. These products are still edible and potentially suitable for human consumption; however, they are destined for elimination or disposal due to economic and aesthetic reasons or to their proximity to the consumption/expiration date. Data relating to this practice, unfortunately widespread, are disconcerting; it is estimated

Department of Chemistry "Giacomo Ciamician"– The University of Bologna, via F. Selmi 2, 40126, Bologna, Italy. E-mail: silvia.panzavolta@unibo.it, simone.dagostino2@unibo.it

† Electronic supplementary information (ESI) available: Crystal data tables, powder XRD patterns, thermal analyses, FTIR spectra, and stress–strain curves. CCDC 2306305–2306309. For ESI and crystallographic data in CIF or other electronic format see DOI: **https://doi.org/10.1039/d4me00055b**

‡ Present address: Department of Inorganic Chemistry – University of Granada, Avenida de la Fuente Nueva S/N 18071 Granada, Spain.

§ These authors contributed equally to this work.

¶ Present address: University College Cork, T12 YN60, Cork, Ireland.

that 30 to 50% of the food produced never reaches the consumer's table.[1,2]

The loss and waste of food is not only an ethical issue, but also involves a significant waste of resources in the production process.[2–4]

The 'cold chain' is vital for perishable goods and pharmaceuticals, ensuring quality and safety from production to sale by controlling the temperature during transportation and storage. Proper temperature management minimizes spoilage risk, extends shelf life, and guarantees product safety.

According to the Hazard Analysis and Critical Control Points (HACCP) standards, foods are categorized by temperature requirements: chilled (0 °C to 15 °C), frozen (−18 °C to −25 °C), and deep-frozen (below −25 °C). For instance, meat and cheese should be stored at 4–6 °C, while fruits and vegetables require temperatures below 8 °C.[5] The global cold chain market was valued at $270 billion in 2021 and is projected to grow at a compound annual rate (CAGR) of 18.6% from 2023 to 2030.[6]

Maintaining the right temperature for each food prevents deterioration of the nutritional and organoleptic properties, while defrosting and refreezing can cause the growth and multiplication of undesirable microorganisms and bacteria.[7–9] The same treatment is applied to pharmaceutical products stored at a constant temperature.[10–16]

To date, the most commonly used indicators for reporting temperature violations are based on radio frequency identification (RFID) and time–temperature indicator (TTI) tags, capable of signaling when a given threshold temperature has been reached or exceeded,[17–20] or disposable colorimetric sensors.[21,22] Digital devices are costly and complex, often unsuitable for individual products. On the other hand, colorimetric sensors offer affordable and user-friendly monitoring without the need for read-out devices or trained personnel,[21,22] whereas most of the indicators on the market are based on pigments/mixtures that degrade with increasing temperature, posing, thus, limits on reutilization. Alternatives based on nanoparticles that exhibit fluorescence changes due to temperature variations have been proposed recently in the literature;[21–24] however, their synthetic procedures and implementation into devices remain pretty challenging. Therefore, finding affordable and easy-to-synthesize materials for colorimetric sensors in the cold chain is crucial. In this regard, thermo- and photochromic molecules are promising candidates since they undergo a color change when heated above a threshold temperature or upon irradiation with visible or UV light.[14,25,26]

Among thermo- and photochromic compounds, *N*-salicylideneanilines, also named anils, and their derivatives have received particular attention due to the ease of preparation and their ability to switch, depending on the stimulus applied, between three different forms: a pale yellow enol form, a colorless *cis*-keto form, and an orange-red *trans*-keto form,[26–28] as depicted in Fig. 1.

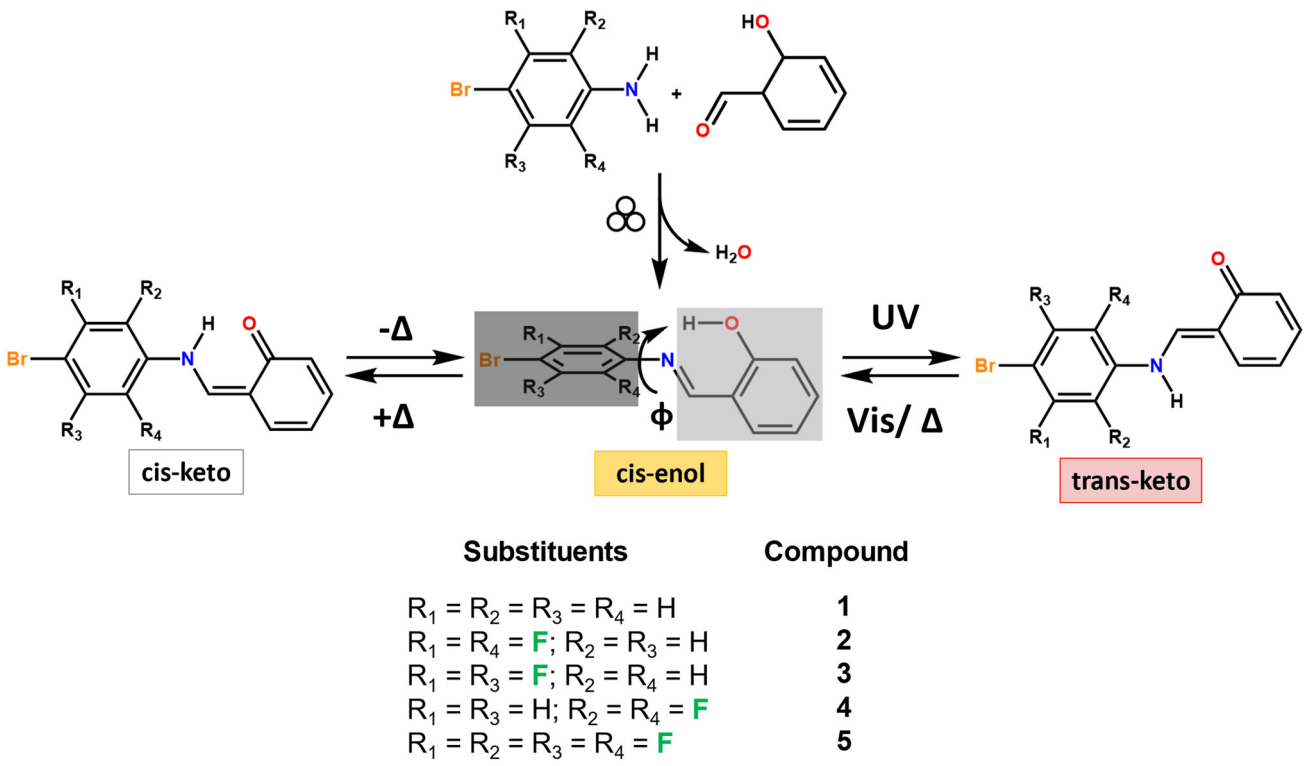

Fig. 1 Mechanochemical synthesis and chemical structure of the *N*-salicylideneaniline compounds studied in this work and the general pathway for the thermo- and photochromic processes in anil; the variability in the dihedral angle (φ) is associated with the chromic behavior.

In the solid state, most anil compounds have a thermochromic behavior, whereas photochromism is rarely observed in these systems. As a rule of thumb, photochromism is usually observed for non-planar anils, characterized by a dihedral angle $\varphi \geq 30°$ between the aromatic ring planes. Quasi-planar conformations ($\varphi \leq 20°$) tend to exhibit thermochromic features, whereas for φ values between 20° and 30°, the compound can display both behaviors (see Fig. 1).[27,29–32] However, a number of studies have shown the limit of such an empirical rule.[33–36] Photochromism is the preferred choice for developing a suitable sensor for the cold-chain, especially when the color change, *e.g.*, from white to red/orange, is marked and easily naked eye-detectable, and the back reaction is slow or virtually negligible at low temperature. In contrast, thermochromic solids tend to quickly change their color with temperature variations.

According to the proposed "pedal-motion" mechanism of *cis–trans* photoisomerization, photochromism should be observed only when there is sufficient reaction volume for the molecule to undergo the isomerization process within the crystal.[31,37]

The main strategies currently used to design and modify materials properties rely either on a crystal engineering approach,[28,30,38–40] *i.e.* a search for co-crystals or polymorphs, or on covalent modifications, namely, the introduction of substituents able to act as space closers/openers[41,42] or to alter the torsional angle φ,[43,44] thus enabling the *cis–trans* photoisomerization. In this regard, functionalizing the aniline residue offers several possibilities.

Intermolecular C–F···H–C interactions occurring in the crystal structures of organofluorines[45,46] play an important role in directing supramolecular assembly in chemical and biological systems.[45,47–49]

Moreover, in contrast to the C–F···F–C ones, whose directionality is insignificant,[45,50] they can be exploited to lock in place the adjacent bromoaniline residue through the establishment of self-complementary interactions, which, in combination with the repulsive character of the C–H···H–C and C–F···F–C interactions, can result in a change of the torsional angle (φ) which can be exploited to favoring thermo or photochromism.

Additionally, the enlargement of the electropositive σ-hole localized on the Br-atom,[51–53] through the increasing number of F-atoms on the aniline residue, may give rise to halogen bonding interactions (XB)[54,55] of the type X···X,[56,57] thus influencing the relative molecular arrangement within the solid products.

The aim of this research was manifold: on the one hand, we were interested in synthesizing a new family of anils bearing different numbers of H/F substituents on the bromoaniline residue (see Fig. 1) and seeing how the H/F ratio affects the chromic features in solids. Five anil compounds were synthesized *via* mechanochemistry, with an eye on green chemistry principles,[58,59] and thoroughly characterized through a combination of X-ray diffraction (XRD), thermal techniques including differential scanning calorimetry and thermogravimetric analysis (DSC and TGA), and infrared spectroscopy (FTIR). The best candidate was then selected and embedded in carboxymethyl cellulose (CMC), a non-toxic, biodegradable and GRAS (generally recognized as safe) biopolymer; the photochromic composite film thus obtained was further characterized *via* XRD, thermal and mechanical techniques.

UV irradiation of the composite film resulted in a color change from the yellowish *cis*-enol form to the red *trans*-keto form stable at −19 °C and 4 °C; the reverse process was monitored with UV-vis spectroscopy at −19 °C, 4 °C and room temperature. At RT, the color fades completely in approximately four days, making, *de facto*, the selected compound a suitable pigment to be used in the cold chain for long transportation or in all cases for which a rapid visual inspection of the storage conditions is desirable.

2. Materials and methods

All reactants and reagents were purchased from Sigma-Aldrich and used without further purification. Reagent grade solvents and Milli-Q water were used. All acronyms and compound names are listed in Table 1.

2.1 Synthesis

For the synthesis of compounds **1–5**, 100 μL (0.95 mmol) of salicylaldehyde was co-ground manually for *ca.* 20–30 minutes in a ball-milling apparatus (Retsch MM 200) operating at 20 Hz for 20 minutes with one equivalent (0.95 mmol) of the corresponding bromoaniline. When the reaction did not reach completion, a slight excess of aldehyde was added, to compensate for the loss of aldehyde due to evaporation during the manual grinding process. Recrystallizing of the so-obtained powders from hot ethanolic solutions left to cool down slowly in the dark afforded single crystals suitable for XRD.

2.2 NMR spectroscopy

^{1}HNMR and ^{13}CNMR spectra were recorded on a Varian INOVA 400 (400 MHz) spectrometer using, as a solvent,

Table 1 List of all the acronyms used in this manuscript

1	4-Bromo-*N*-salicylideneaniline
2	4-Bromo-2,5-difluoro-*N*-salicylideneaniline
3	4-Bromo-3,5-difluoro-*N*-salicylideneaniline
4	4-Bromo-2,6-difluoro-*N*-salicylideneaniline
5	4-Bromo-2,3,5,6-tetrafluoro-*N*-salicylideneaniline
CMC	Carboxymethyl cellulose
CMC-**5**@*x*%	Carboxymethyl cellulose with **5** incorporated at *x*% in weight (*x* = 1, 5, 10, and 15)
NMR	Nuclear magnetic resonance spectroscopy
SCXRD	Single crystal X-ray diffraction
PXRD	Powder X-ray diffraction
TGA	Thermogravimetric analysis
DSC	Differential scanning calorimetry
FTIR	Fourier transform infrared spectroscopy
UV-vis	Ultraviolet and visible electronic absorption spectroscopy
HSM	Hot stage microscopy
HACCP	Hazard analysis and critical control points

chloroform-d_1 (DMSO-d_6) bought from Sigma-Aldrich. See Fig. S1–S5.†

2.3 CMC-5@15% film preparation

300 mg of carboxymethyl cellulose sodium salt (CMCNa) was dissolved in 6 mL of Milli-Q water (5% w/v) and stirred overnight. Subsequently, 45 mg of compound **5**, previously ball-milled at 5 Hz for 90 minutes, was added and the resulting suspension was left under stirring for another 3 hours. The mixture was then ultrasonicated in an ELMASONIC S15H bath filled with water operating at a frequency of 37 kHz for 5 minutes to increase the homogeneity of the dispersed polycrystalline powders, and finally cast into a petri dish with a diameter of 10 cm. Upon evaporation of the solvent, films with a thickness of about 100 μm were obtained. The film thickness was measured using a hand-held digital micrometer (Mitutoyo, Japan) at six different positions in each specimen to an accuracy of 0.001 mm. The obtained films had comparable thicknesses.

2.4 Crystal structure determination

Single-crystal data for compounds **1–5** were collected at RT on an Oxford X'Calibur S CCD diffractometer equipped with a graphite monochromator (Mo-Kα radiation, λ = 0.71073 Å). In the case of crystals showing twinning, reflection data were integrated with the default configuration for twinned crystals of the CrysAlisPro Software. Subsequent structural solution and refinement were performed using the HKLF4 file containing non-overlapped reflections. The structures were solved with SHELXT[60] by intrinsic phasing and refined on F^2 with SHELXL[61] implemented in the Olex2 software[62] by full-matrix least squares refinement. H_{OH} atoms were either directly located or, when not possible, added in calculated positions; H_{CH} atoms for all compounds were added in calculated positions and refined riding on their respective carbon atoms. All non-hydrogen atoms were anisotropically refined and the rigid-body RIGU restraints applied.[61] Data collection and refinement details are listed in Table S1.† The program Mercury[63] was used for molecular graphics and calculation of intermolecular interactions.

2.5 Powder XRD measurements

For phase identification and variable temperature purposes, powder X-ray diffractograms were collected in the Bragg–Brentano geometry, in the 2θ range of 5–40°, on a PANalytical X'Pert PRO automated diffractometer equipped with an X'Celerator detector and using Cu Kα radiation without a monochromator (step size 0.02°; time per step 20 s; 0.04 rad Soller; 40 mA × 40 kV). The program Mercury[63] was used to calculate the powder X-ray patterns based on single crystal data collected in this work or retrieved from the CSD.[64] In all cases, the identity between polycrystalline samples and single crystals was always verified by comparing experimental and calculated powder diffraction patterns (see Fig. S6–S9†).

2.6 Thermogravimetric analysis measurements

TGA measurements were performed with a PerkinElmer TGA7 instrument in the temperature range of 40–300 °C, under a nitrogen flow at a heating rate of 5.00 °C min^{-1}.

2.7 Differential scanning calorimetry measurements

DSC measurements were performed with a PerkinElmer Pyris Diamond DSC instrument. Samples (3–5 mg) were placed in open aluminum pans. Heating was carried out for all samples at 5.00 °C min^{-1} under a N_2 atmosphere.

2.8 Hot stage optical microscopy

HSM analyses were carried out using a Linkam TMS94 device connected to a Linkam LTS350 platinum plate and equipped with polarizing filters. Images were collected with a NIKON DS FI3 camera, from an Olympus BX41 stereomicroscope.

2.9 Fourier-transform infrared spectroscopy

FTIR spectra were recorded in transmission mode on a Bruker Alpha FTIR spectrometer. 1–2 mg of each sample was finely dispersed in *ca.* 200 mg of dry KBr pellets with a diameter of 1.3 cm.

2.10 Mechanical properties

Tensile tests were performed on strip-shaped samples (5 mm width and 40 mm length) using a 4465 Instron dynamometer equipped with a 100 N load cell. The thickness was evaluated with a Mitutoyo micrometer. Stress–strain curves were recorded at a crosshead speed of 5 mm min^{-1} using the software Bluehill Universal for Windows. At least seven specimens were tested for each composition. The stress at break (σ_b) and the strain at break (ε_b) were evaluated and reported with the standard deviation.

2.11 Solid-state UV-irradiation

Samples in KBr pellets or polymeric films placed at a distance of 5 cm were irradiated for 10 minutes using a UV-LED LED EnginLZ1-10UV00-0000 centered at λ = 365 nm (FWHM = 25 nm) and operated at 4.5 V and 700 mA with a radiant flux (φ) of 1200 mw.

2.12 Ultraviolet-visible spectroscopy

The UV-vis electronic absorption spectra of the CMC polymeric films containing finely dispersed photochromic compound **5** were recorded using a Varian CARY 5 UV-vis spectrophotometer in the range of 300–800 nm. The films were cut into 1 cm wide rectangular strips and then inserted into the instrument sample holder. The color fading kinetics were studied utilizing commercial refrigerators/freezers set at 30% relative humidity (RH). The fading trials were replicated twice using distinct film samples. Irradiation cycles were employed to rule out UV-induced degradation and gauge the reproducibility of the photochromic reaction, monitoring

absorbance at 470 nm in single-point mode. Additionally, irradiation cycles were employed to evaluate errors in UV-vis measurements, resulting in a standard deviation (σ) of ±0.002.

3. Results and discussion

3.1 Mechanochemical synthesis and powder diffraction

In a typical mechanochemical synthesis, salicylaldehyde and the respective bromoaniline derivatives were manually co-ground, and the progress of the reaction was monitored by powder X-ray diffraction (XRD) analysis; no solvent addition was required to facilitate the reaction, as the bromoaniline derivatives are liquid. The resulting solids were then recrystallized in the minimum amount of solvent, and the single crystals obtained were analyzed *via* XRD.

In general, the experimental powder XRD patterns of all five mechanochemistry outcomes are significantly different from those of the reagents and can be superimposed to the ones calculated on the basis of the structures obtained from single crystal X-ray diffraction (see Fig. S6–S9†); we can therefore conclude that the synthesis by grinding is successful for all five compounds selected. In some syntheses, the patterns obtained by grinding contained some small peaks attributable to the reactant, and this is possibly due to the volatility of salicylaldehyde at RT; in those cases, adding a slight excess of salicylaldehyde was necessary to obtain the desired product in the pure form. On the other hand, when the same syntheses were carried out in a ball milling apparatus, no salicylaldehyde excess was required, and a quantitative reaction could be obtained with a stoichiometric ratio of the reactants. Fig. 2 depicts the PXRD patterns of the reactants and mechanochemical product in the case of compound **5**.

3.2 Structural and chromic features

Single crystal diffraction reveals that the molecular structures of the five obtained compounds are all quite similar. An analysis of the C–O and C–N distances confirms the formation of the more thermodynamically stable *cis*-enol form in all cases, and, as expected, all compounds feature the presence of an intramolecular hydrogen bond[65,66] between the –OH and the –C═N– functions; besides this, also weak intermolecular interactions of types C–H···O and C–F···H are detected (see Fig. 3 and Table 2). Despite the increasing number of F atoms, along the series **1**–**5**, no occurrence of significant X···X bonds is observed. Instead, this feature affects the stacking pattern of the molecules, see Fig. 4. Compounds **1** and **2** form head-to-head piles, whereas in **3**, **4** and **5** there are head-to-tail stackings.

In general, the interplay between weak intermolecular interactions and stacking accounts for the modification of crystal packing and torsional angle (φ).

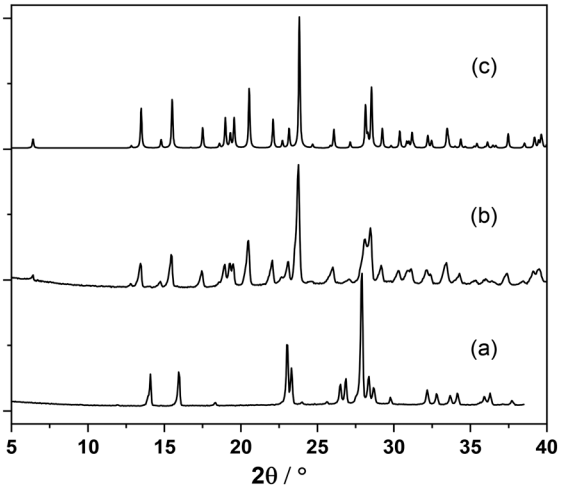

Fig. 2 Powder XRD patterns of mechanochemical synthesis of compound **5**. (a) Tetrafluorobromoaniline experimental pattern, (b) tetrafluorobromoaniline ground with 1 equivalent of salicylaldehyde, and (c) calculated powder pattern for crystalline **5**.

3.3 Thermal and photochromic properties

As shown by thermal analyses (see Fig. S10 and S11† for TGA and DSC traces, respectively, and Table S2† for DSC data), all compounds present good stability, with an endothermic peak after 100 °C corresponding to melting, whereas degradation starts at *ca.* 150 °C in each case.

The thermo- and photochromic properties were verified by lowering the temperature and irradiating with UV (λ = 365 nm) single crystal samples of compounds **1**–**5**. As witnessed by the slight thermal fading (pale yellow → colorless), all five compounds possess a weak thermochromic character (see Fig. 5 for compound **5**).

As expected, compounds **1** and **5**, with a torsional angle greater than 20° (Table 2), confirm the hypotheses previously made and, upon UV irradiation, show a very intense and rapid color variation, from white/yellowish to red, associated with the conversion into the corresponding *trans*-keto forms. Compounds **2** and **4**, which possess planar structures, are not photochromic; in contrast, compound **3**, also planar, displays only a weak color change after prolonged (>30 min) UV irradiation. After irradiation, all specimens were again analyzed *via* X-ray diffraction: despite the color variation, visible to the naked eye, no significant changes were found in the crystal structures, as the unit cell parameters and C–O and C═N bond distances were the same as those observed before irradiation.

Photochromic compounds **1**, **3**, and **5** were irradiated and maintained at 100 K for single crystal analysis. However, no structural changes were detected. The authors suppose therefore that the interconversion between the species is only superficial: the UV light can only radiate through the first few layers of the crystals, and conversion to the *trans*-keto form is accompanied by some amorphization.

Infrared spectroscopy (FTIR) was then used to assess the formation of the *trans*-keto form responsible for the red

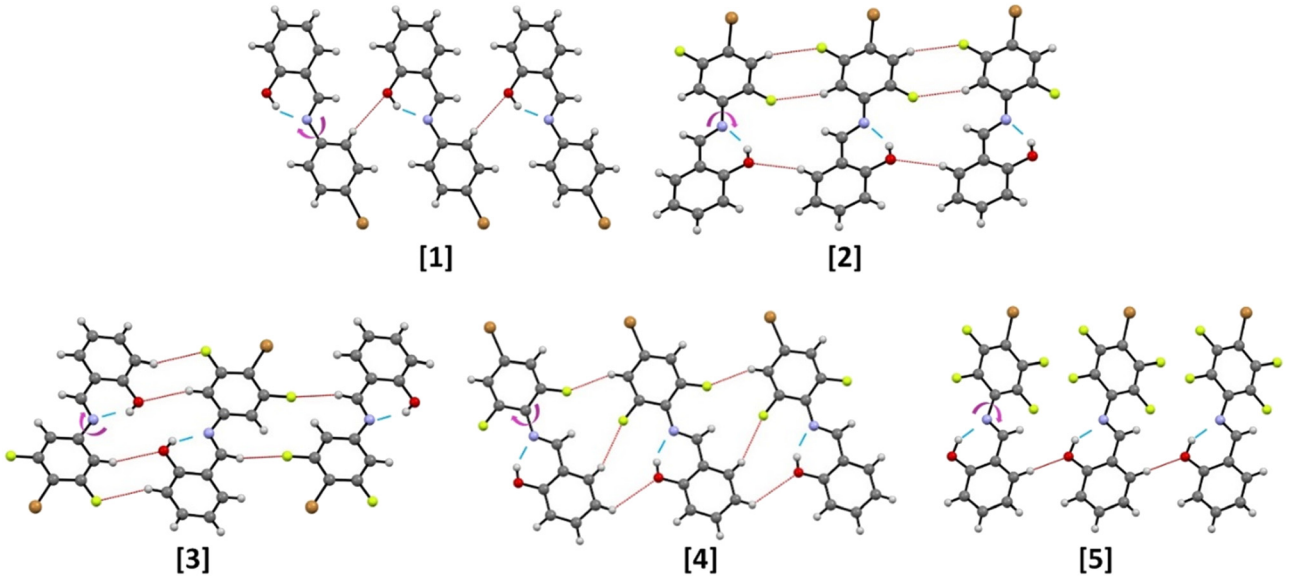

Fig. 3 Molecular structures of compounds **1**–**5**, as determined from single crystal XRD analysis. The intramolecular hydrogen bonds are shown in blue, whereas weak C–H···O and C–F···H intermolecular interactions are depicted in red, and the torsional angle (φ) is displayed with a pink arrow.

Table 2 Relevant intra- and intermolecular hydrogen bond distances (Å), C–OH and C═N bond distances (Å), and torsional angles (°) in crystalline **1**–**5** calculated from the program Mercury[64]

Entry	O(H)···N	C(H)···O	C(H)···F	C–OH	C═N	φ	Expected behavior
1	2.593(9)	3.427(9)	—	1.35(1)	1.29(1)	38	Photochromic
2	2.58(2)	3.37(2)	3.48(2)	1.34(2)	1.28(2)	5	Thermochromic
3	2.624(5)	3.484(5)	3.523(5)	1.343(5)	1.263(5)	4	Thermochromic
4	2.596(3)	3.535(5)	3.273(5)	1.343(5)	1.270(5)	4	Thermochromic
5	2.619(7)	3.565(9)	—	1.353(9)	1.282(9)	47	Photochromic

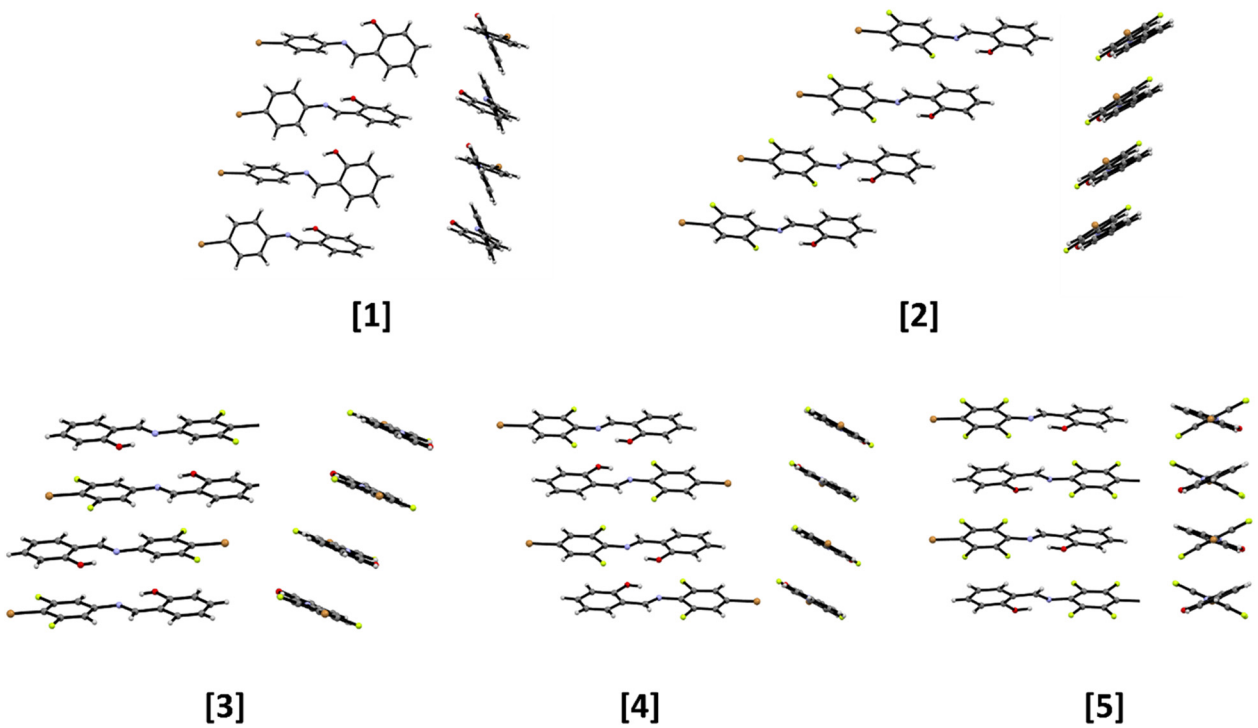

Fig. 4 Front and side views of the molecular stackings detected within crystalline compounds **1**–**5** highlighting the torsional angles between the aromatic moieties arising from the different interaction patterns detected from structural analysis.

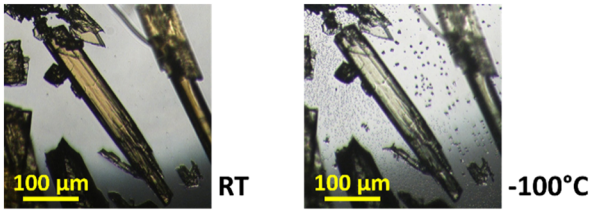

Fig. 5 Visual comparison of color changes for crystals of compound **5** taken at RT and −100 °C.

coloring in photochromic compounds. The three photochromic compounds were dispersed in KBr pellets (*ca.* 2% in weight) and subjected to UV irradiation (LED at 365 nm) to evaluate the presence of the *trans*-keto form within their crystals.

In compound **1**, the back reaction is fast, and the *trans*-keto form reverts quickly to the *cis*-enol form; persistence of the red color can only be observed upon steady UV irradiation. Conversion to the keto-form in solid **3** could only be observed by visual inspection, as the product is likely present in quantities below the detectable limit. On the other hand, the red color observed with compound **5** is maintained for about 90 minutes when the solid is stored under ambient light and temperature conditions. As shown in Fig. 6, the color change is indeed accompanied by a marked variation in its spectrum: the band at 1620 cm^{-1} (ascribed to the C═N stretching of the enol form) decreases, while the appearance of a band at 1670 cm^{-1}, the region where the stretching of conjugated C═O falls,[29,67] confirms the formation of the *trans*-keto tautomer product. After thermal treatment (80 °C, 20 min) or after exposure to visible light (447 nm), the original color is instantaneously recovered, therefore the process is reversible (see the movie in the ESI†). Fig. S14† shows the behavior for the other compounds.

3.4 Composite cellulose film preparation

Based on this preliminary screening, we concluded that compound **5** is the best candidate to incorporate in the CMC-polymeric film to obtain a membrane with photochromic properties. To this end, a polycrystalline sample of **5** was finely ground for 90 minutes with ball milling at a frequency of 5 Hz to maximize the homogeneity of the crystalline powder, which was then incorporated in the polymeric matrix.

By varying the amount of compound **5**, it was possible to optimize the color intensity obtained upon irradiation with visible light: four different weight percentages of **5** (1, 5, 10 and 15%) were suspended in CMC, providing four different composite film formulations labelled CMC-**5**@1%, CMC-**5**@5%, CMC-**5**@10% and CMC-**5**@15%, respectively. These films were irradiated at λ = 365 nm for 10 minutes, with the UV lamp positioned at 5 cm from the film; the films were then stored at 4 °C up to 30 days.

As shown in Fig. 7, only in the films CMC-**5**@10% and CMC-**5**@15% the red color was intense and persistent over time: samples stored at 4 °C for 30 days fully retained their coloring. Given the higher intensity of red staining and the

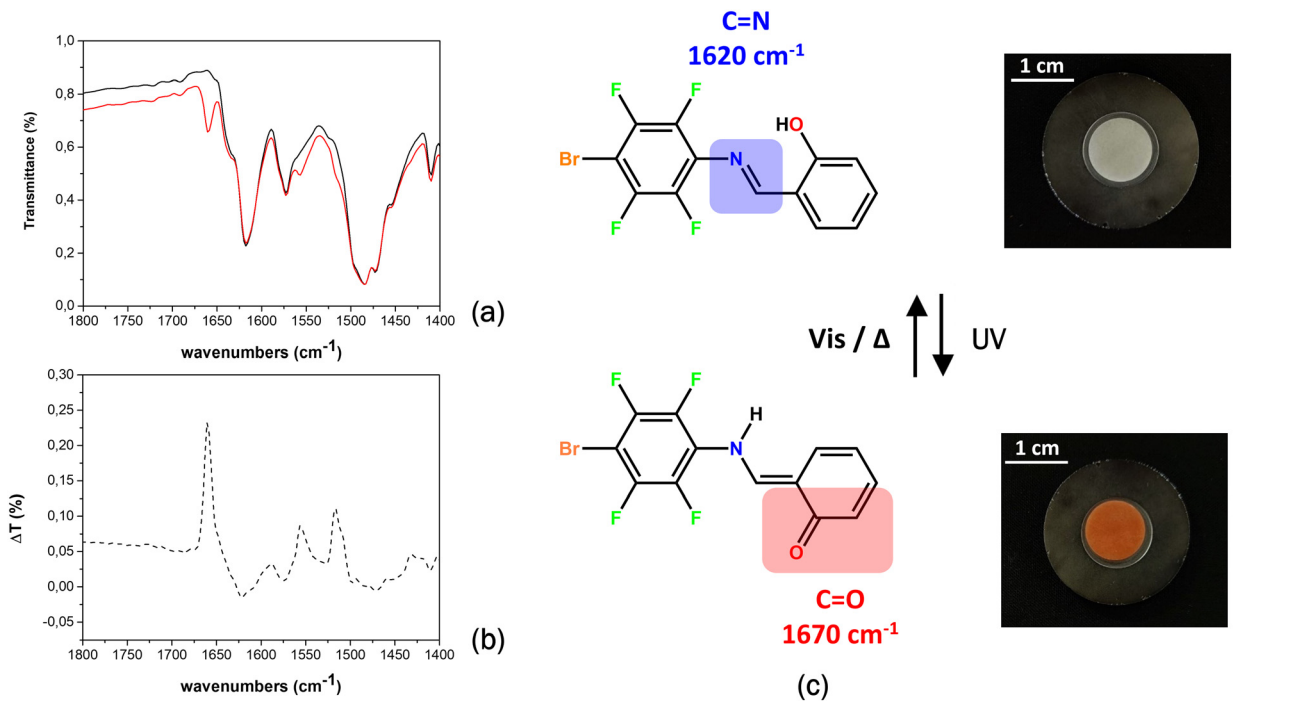

Fig. 6 (a) Details of the FTIR spectra run before (black line) and after UV irradiation (red line), (b) difference spectrum between the untreated and the irradiated samples, and (c) the *cis*-enol ↔ *trans*-keto equilibrium occurring within crystalline **5** and photographs of the non-irradiated and irradiated KBr pellets used for the FTIR measurements.

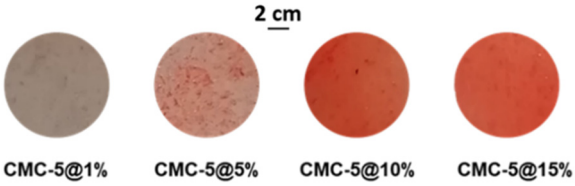

Fig. 7 Micrographs of CMC-based films containing, from left to right, increasing amounts of compound **5**, showing how composite film homogeneity is reached at higher concentrations.

better homogeneity of **5** in the film, the CMC-**5**@15% composite was selected for further testing.

Fig. 8a compares the thermograms for a pristine CMC film, a composite CMC-**5**@15%, and pure **5**, showing that the photochromic compound has been successfully embedded in the polymeric film. In the thermogravimetric plot for the composite, three weight losses can be detected: the first one at around 50 °C corresponding to the evaporation of surface water; the second one starting at 130 °C, attributable to the degradation of crystalline **5**, and the third one beginning at 260 °C due to carboxymethyl cellulose degradation. DSC measurements were conducted to study the thermal behavior of photochromic film CMC-**5**@15% between the temperature range of −25 °C and 200 °C (Fig. S12†). The results of the DSC measurements were consistent with TGA, indicating that the thermal behavior of the film is a superimposition of the behaviors of its two components, *i.e.*, dehydration of CMC followed by the melting of compound **5**. At the same time, no significant processes were observed at lower temperatures. Heating and cooling cycles within the same range were also performed on CMC-**5**@15%. The reproducibility of the traces ensures that any possibility of sample degradation can be dismissed (Fig. S14†). Powder XRD measurements (Fig. 8b) further confirm the doping of **5** in the CMC membrane, as all the characteristic peaks of pure crystalline **5** can be observed in the measured pattern, despite the preferred orientation of the powders in the cellulose film affecting intensities in the PXRD pattern.

The mechanical properties of the pristine CMC and of the film obtained after mixing of the biopolymer with **5** have been evaluated by tensile stress–strain tests. By comparing the stress–strain curves (Fig. S15†), the similar shape and the complete superimposition at a few percent of deformation indicate that the presence of CMC dominates the mechanical behavior, and the crystal addition predominantly reduces the stress at break (29 ± 9 MPa and 55 ± 6 MPa, for CMC and CMC-**5**@15%, respectively) of the films without affecting their brittleness. The mechanical characteristics necessary for the proposed application are thus preserved.

3.5 Photochromic features in the composite film

The absorption spectra of CMC-**5**@15%, before and after UV irradiation, were also registered and are shown in Fig. 9. The non-irradiated film shows a distinct broad absorption band extending below λ = 430, which, in analogy with literature reports,[32,34,68,69] can be attributed to the n–π* absorption of the *cis*-enol form and to the absorption of the CMC. UV irradiation causes an increase of the absorption in the λ = 400–600 nm region, and the presence of the band at 470 nm indicates the presence of the *cis*-keto tautomer, in agreement with the photochromic behavior observed in FTIR spectroscopy.

The absorption spectrum, initially recorded before irradiation at 365 nm, undergoes complete restoration when the film is irradiated again at room temperature with a blue LED emitting light at 447 nm. To evaluate the compound's stability and reproducibility, 11 cycles were executed, as illustrated in Fig. 9.

Thermal fading of staining was further evaluated with UV-vis spectroscopy by monitoring the absorption intensity at 470 nm of irradiated CMC-**5**@15% film strips, stored at three different temperatures (−19 °C, 4 °C and RT); in all cases the relative humidity, RH, was 30%. Remarkably, even at sub-

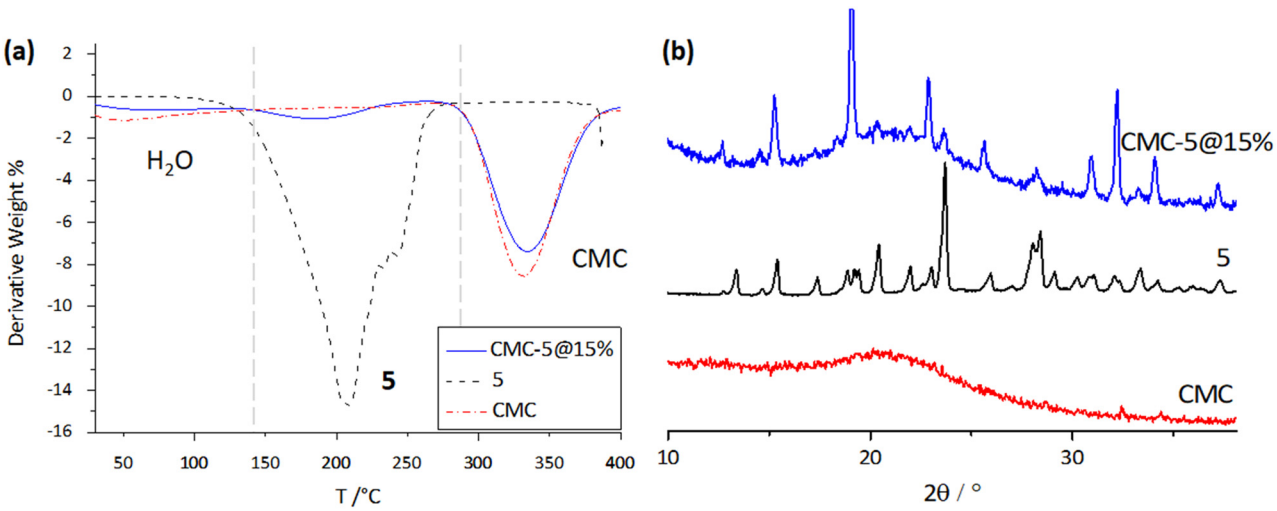

Fig. 8 (a) TGA thermograms (left) and (b) powder XRD patterns for the pristine CMC film, pure **5**, and the CMC-**5**@15% composite.

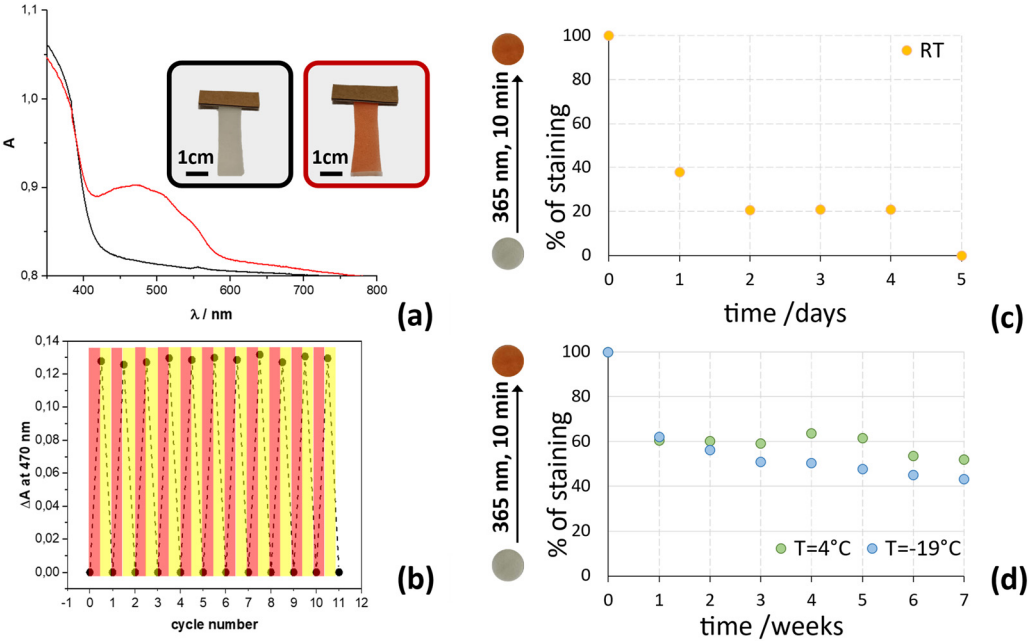

Fig. 9 (a) Absorption spectra of the CMC-**5**@15% composite photochromic film before (black line) and after UV irradiation (red line), and photographs of the strip used for the measurements. (b) Absorbance variation measured at 470 nm of the CMC-**5**@15% film subjected to UV irradiation (red areas: irradiation at 365 nm; yellow areas: irradiation at 447 nm). Thermal fading of sample CMC-**5**@15% monitored at 470 nm at different temperatures: (c) room temperature up to 5 days; (d) 4 °C and −19 °C up to 7 weeks (0% corresponds to the absorbance of non-irradiated CMC-**5**@15%; 100% corresponds to the absorbance of just-irradiated CMC-**5**@15%).

freezing temperatures (−19 °C), the color change induced by irradiation at 365 nm was easily noticeable to the naked eye. Importantly, there was no ice formation that obscured its visibility or affecting the composite film under sub-freezing conditions, contrasting with occurrences in other reported systems.[70] The thermal fading curves at different temperatures are reported in Fig. 9b and reveal that the composite film CMC-5@15% can maintain its staining after irradiation with UV light for several weeks only if stored at temperatures below 4 °C. Indeed, the film strips preserved at −19 °C and 4 °C have maintained high staining (>40%) even after 7 weeks (50 days). In contrast, when the film is stored at room temperature (about 19 °C), its coloring decreases much more quickly, reaching a reduction to less than 40% in absorption values already after one day and of 20% within 2 days, showing equal to pre-irradiation values in about 5 days.

These results indicate that the photochromic film exhibits comparable performance at temperatures of −19 °C and 4 °C, lacking the ability to effectively discriminate temperature differences below 4 °C. In contrast, the film demonstrates consistent and reliable color changes in response to room temperature fluctuations, suggesting that it could be an excellent candidate as a sensor for monitoring refrigerated products within the 0–15 °C temperature range. Taking advantage of the film's ability to visually indicate temperature excursions, companies can improve quality control measures and ensure compliance with temperature sensitive storage requirements in the cold chain.

To obtain information on the effect of temperature changes over time on the film's staining changes and to evaluate its applicability as a sensor at a set of temperatures commonly encountered, further experiments were carried out. The photochromic film samples were subjected to irradiation followed by storage in the dark at 15, 25, and 32 °C. The hourly evaluation of color fading using UV-vis measurements was recorded post-irradiation by monitoring changes in the intensity of the peak centered at 470 nm.

The peak intensity at 470 nm recorded at t_0 (film just irradiated) was considered as 100%, while that of the curve recorded after the complete fading of the staining (which overlaps that of the non-irradiated film) has been taken as 0%, as shown in Fig. 10 for the film at 15 °C.

The color fading kinetics revealed significant variations depending on temperature conditions. A pronounced change in film staining occurred within the initial hours of exposure to different temperatures. At 32 °C, the film showed a 50% reduction in staining already within 2 hours, and within 4 h if stored at 25 °C, while it took about 1 day at 15 °C. These results confirm previous observations at room temperature (about 19 °C) and emphasize the potential of the film to visually indicate thermal history. Indeed, these results suggest that photochromic films can serve as effective indicators of temperature excursions in cold chain applications: a staining decrease below 75% of the initial intensity is readily discernible to the naked eye, enabling quick assessment of temperature deviations. Leveraging this property, we propose a labelling system incorporating the photochromic film as a 'sensor' on product packaging or containers (Fig. 11).

The legend presents three different intensities: one relative to the maximum intensity of coloration, equivalent to

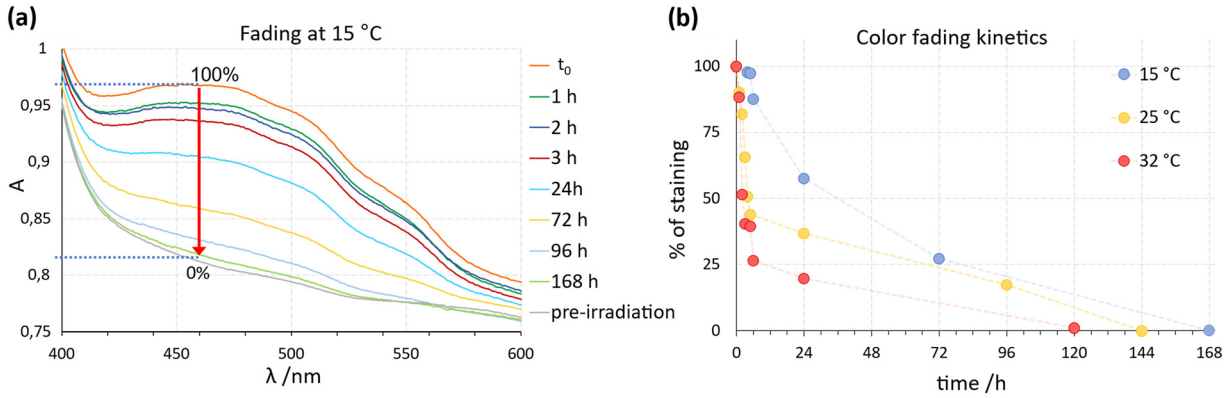

Fig. 10 (a) UV-vis spectra recorded at different times after the irradiation of the film stored at 15 °C, which show the decay kinetics of the film staining: 100% refers to the absorbance at 470 nm of the just-irradiated film at t_0, while 0% refers to the film absorbance after several days, when the staining and the peak at 470 nm disappeared (the curve overlaps again with that of the non-irradiated sample). (b) Color fading kinetics of films stored at 15 (blue), 25 (orange) and 32 °C (red) referred to the fading of the peak at 470 nm.

100% (just-irradiated film), one relative to 50% of the sensor intensity, while the third one indicates the intensity of coloration when the film has already faded. By comparing the film's staining with the predefined legend, users can easily ascertain if temperature guidelines have been maintained. For instance, matching the 'happy face' color indicates compliance, while matching the 'neutral face' suggests deviations, such as prolonged exposure to above 15 °C for approximately 24 hours or within the range of 25–32 °C for 2–4 hours. This innovative approach holds promise for enhancing cold chain management practices and safeguarding product quality.

The unique properties of photochromic films open a multitude of potential applications in cold chain management: a promising path is their use in national or same-day ground transportation services. The ease of preparation and low production costs associated with these materials make them particularly attractive to small and medium-sized enterprises looking for cost-effective solutions to monitor their transport operations and ensure compliance with cold chain management.

Compared to existing sensors on the market, which can be prohibitive for small businesses, photochromic films, thanks to the low costs of raw materials and ease of preparation, are attractive for small and medium-sized enterprises looking for cost-effective solutions to monitor their transport operations and ensure compliance with cold chain management. This accessibility and ease of use, coupled with their reliability in indicating temperature excursions, position them as a turning point for companies aiming to support the integrity of their goods during transit.

In addition, the scalability of production processes for CMC films[71] could facilitate integration into existing supply chain workflows. Whether tracking perishable goods over short or long distances, these films offer a versatile solution that can be adapted to various transport modes and logistics scenarios.

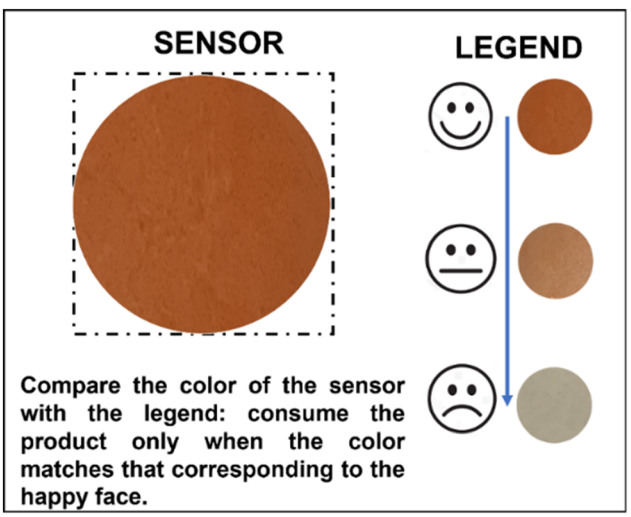

Fig. 11 This sketch shows an example of a tag containing the photochromic CMC-5@15% composite film capable of acting as a cold chain tracker. The tag's legend shows whether the product has been adequately transported.

4. Conclusions

The outcomes of this study are in line with the goal stated in the introduction, that is to investigate and explore new thermo- and photochromic compounds that can be utilized as active components for making temperature colorimetric indicators. These types of indicators can help to visually track the cold chain and mitigate food losses caused by improper maintenance of the cold chain during transportation.

To this end, five salicylaldehyde derivatives (**1**–**5**) bearing different ratios of H/F substituents on the aniline residue were designed and synthesized *via* mechanochemical methods and thoroughly characterized *via* XRD and thermal analyses. All solids showed pale and reversible thermochromism whereas crystalline **1**, **3**, and **5** showed photochromic properties when irradiated under UV light, with a marked change in color attributed to the interconversion from the *cis*-enol to the

trans-keto tautomer, as confirmed by infrared spectroscopy (FTIR). Regarding the aim of this research, compound **5** showed the best performances in terms of color change, persistency and fading dependence on the ambient temperature. Compound **5** was, further, embedded in a non-toxic, biocompatible carboxy methyl cellulose polymer, and a composite photochromic film was produced. As the color hue and intensity remained dependent on the external temperature and the changes were appreciable by simple visual inspection, the composite was tested for potential application in the cold chain by studying the color fading at three different temperatures: −19 °C, 4 °C and RT. The results showed that, when stored below 4 °C, the composite film retained its red color for over 7 weeks. At room temperature (19 °C), however, a rapid decline in color intensity occurred, from 40% of the initial value after 1 day. Further experiments were performed at constant temperatures (15 °C, 25 °C, and 32 °C) to simulate material exposure under varied environmental conditions. Results showed that the fading rate increased proportionally with temperature, with a 50% reduction in coloration observed within 2 hours at 32 °C, within 4 hours at 25 °C, and 22 hours (about 1 day) at 15 °C.

These characteristics make this photochromic film potentially suitable for the transport of refrigerated products, which generally require a transport temperature between 0 and 15 °C, and it can represent a potential alternative to electronic devices such as radio frequency identification (RFID) and time–temperature indicators (TTIs) or to other non-reusable colorimetric sensors based on degradable pigments or nanoparticles.

Overall, these results demonstrate, as a proof of concept, that films doped with photochromic compounds can be proposed as materials for controlling cold chains in food or drug transportation.

However, the doped photochromic film, presented herein, was studied under laboratory conditions, and further development, *e.g.*, toxicity assessment, scaling up over the gram scale, and tests under real conditions, is required prior to be effectively applied in the cold chain, whereas future optimizations of the formulation could allow the obtainment of a suitable material capable of indicating temperature changes even below 4 °C. Work is ongoing to develop new materials and expand the temperature range detection.

Author contributions

SDA, FG, SP: conceptualization, manuscript preparation and supervision; AA, MFDL, LB, SL: experimentation and data collection; FG: funding acquisition.

Conflicts of interest

There are no conflicts to declare.

Acknowledgements

The authors acknowledge financial support from the University of Bologna (RFO-Scheme).

References

1 J. Parfitt, M. Barthel and S. Macnaughton, *Philos. Trans. R. Soc., B*, 2010, **365**, 3065–3081.
2 FAO, *Global food losses and food waste: extent, causes and prevention*, Food and Agriculture Organization of the United Nations, Rome, 2011.
3 ISPRA AMBIENTE, *Rapporto spreco alimentare: un approcio sistemico per la prevenzione e la riduzione strutturali*, 2018.
4 J. Lundqvist, C. de Fraiture and D. Molden, *Saving Water: From Field to Fork – Curbing Losses and Wastage in the Food Chain*, SIWI Policy Brief, 2008.
5 EU, *Regulation (EC) No 883/2004 of the European Parliament and of the Council of 29 April 2004*, Macmillan Education UK, London, 2015.
6 Grand View Research, *Cold Chain Market Size, Share & Trends Analysis Report By Type (Storage, Transportation, Packaging, Monitoring Components), By Temperature Range, By Application, By Region, And Segment Forecasts, 2024 - 2030*, 2024.
7 T. Gao, Y. Tian, Z. Zhu and D.-W. Sun, *Trends Food Sci. Technol.*, 2020, **99**, 311–322.
8 J.-W. Han, M. Zuo, W.-Y. Zhu, J.-H. Zuo, E.-L. Lü and X.-T. Yang, *Trends Food Sci. Technol.*, 2021, **109**, 536–551.
9 Q.-S. Ren, K. Fang, X.-T. Yang and J.-W. Han, *Trends Food Sci. Technol.*, 2022, **119**, 133–151.
10 N. A. Pambudi, A. Sarifudin, I. M. Gandidi and R. Romadhon, *Energy Rep.*, 2022, **8**, 955–972.
11 C. M. Hanson, A. M. George, A. Sawadogo and B. Schreiber, *Vaccine*, 2017, **35**, 2127–2133.
12 B. F. Hibbs, E. Miller, J. Shi, K. Smith, P. Lewis and T. T. Shimabukuro, *Vaccine*, 2018, **36**, 553–558.
13 W. Huang, X. Wang, J. Xia, Y. Li, L. Zhang, H. Feng and X. Zhang, *Trends Food Sci. Technol.*, 2023, **133**, 189–204.
14 S. Rossi, M. Simeoni and A. Quaranta, *Dyes Pigm.*, 2021, **184**, 108879.
15 T. N. Tikhonova, D. Cohen-Gerassi, Z. A. Arnon, Y. Efremov, P. Timashev, L. Adler-Abramovich and E. A. Shirshin, *ACS Appl. Mater. Interfaces*, 2022, **14**, 55392–55401.
16 Y. Xiao, Z. Tang, X. Huang, W. Chen, J. Zhou, H. Liu, C. Liu, N. Kong and W. Tao, *Chem. Soc. Rev.*, 2022, **51**, 3828–3845.
17 J. Xia, W. Huang, X. Wang, Z. Zhu, M. Zhang and X. Zhang, *Food Control*, 2023, **154**, 109976.
18 B. Ye, J. Chen, H. Ye, Y. Zhang, Q. Yang, H. Yu, L. Fu and Y. Wang, *Food Chem.*, 2022, **373**, 131448.
19 M. Fattori, C. A. M. Da Costa, J. Fijn, E. Genco, P. Harpe, E. Cantatore and M. Charbonneau, in *2020 IEEE Custom Integrated Circuits Conference (CICC)*, IEEE, Boston, MA, USA, 2020, pp. 1–4.
20 S. Wang, X. Liu, M. Yang, Y. Zhang, K. Xiang and R. Tang, *Packag. Technol. Sci.*, 2015, **28**, 839–867.
21 G. Cui, M. Li, A. Qileng, H. Yang, M. Chen, W. Liu and Y. Liu, *J. Mater. Chem. C*, 2023, **11**, 10843–10851.
22 Y.-C. Wang, L. Lu and S. Gunasekaran, *Biosens. Bioelectron.*, 2017, **92**, 109–116.

23 A. Navrotskaya, D. Aleksandrova, M. Chekini, I. Yakavets, S. Kheiri, E. Krivoshapkina and E. Kumacheva, *ACS Nano*, 2022, **16**, 8641–8650.
24 Y. Zou, J. Guo, Y. Liu, Y. Du, Y. Pu and D. Wang, *Polym. Chem.*, 2023, **14**, 1275–1281.
25 M. Maafi, *Molecules*, 2008, **13**, 2260–2302.
26 Y. Li, H. Li, W. Jin, X. Xu, H. Liu, Y. Ding, G. Wang, T. Zhang, Q. Peng, J. He, Q. Hu, L. Pan and K. Li, *Dyes Pigm.*, 2022, **202**, 110295.
27 E. Hadjoudis and I. M. Mavridis, *Chem. Soc. Rev.*, 2004, **33**, 579–588.
28 N. Baus Topić and D. Cinčić, *Cryst. Growth Des.*, 2023, **23**, 6795–6804.
29 A. Carletta, F. Spinelli, S. d'Agostino, B. Ventura, M. R. Chierotti, R. Gobetto, J. Wouters and F. Grepioni, *Chem. – Eur. J.*, 2017, **23**, 5317–5329.
30 K. M. Hutchins, S. Dutta, B. P. Loren and L. R. MacGillivray, *Chem. Mater.*, 2014, **26**, 3042–3044.
31 H. Sugiyama and H. Uekusa, *CrystEngComm*, 2018, **20**, 2144–2151.
32 J. Harada, T. Fujiwara and K. Ogawa, *J. Am. Chem. Soc.*, 2007, **129**, 16216–16221.
33 F. Robert, A. D. Naik, B. Tinant, R. Robiette and Y. Garcia, *Chem. – Eur. J.*, 2009, **15**, 4327–4342.
34 A. Carletta, X. Buol, T. Leyssens, B. Champagne and J. Wouters, *J. Phys. Chem. C*, 2016, **120**, 10001–10008.
35 A. A. Dar and A. A. Ganie, *Cryst. Growth Des.*, 2020, **20**, 3888–3897.
36 R. Koibuchi, I. Yoshikawa and H. Houjou, *J. Phys. Chem. A*, 2022, **126**, 4164–4175.
37 J. Harada and K. Ogawa, *Chem. Soc. Rev.*, 2009, **38**, 2244–2252.
38 G. R. Desiraju, *Angew. Chem., Int. Ed.*, 2007, **46**, 8342–8356.
39 D. Braga, F. Grepioni, L. Maini and S. d'Agostino, *IUCrJ*, 2017, **4**, 369–379.
40 C. B. Aakeröy, N. R. Champness and C. Janiak, *CrystEngComm*, 2009, **12**, 22–43.
41 I. O. Staehle, B. Rodríguez-Molina, S. I. Khan and M. A. Garcia-Garibay, *Cryst. Growth Des.*, 2014, **14**, 3667–3673.
42 A. Carletta, M. Colaço, S. R. Mouchet, A. Plas, N. Tumanov, L. Fusaro, B. Champagne, S. Lanners and J. Wouters, *J. Phys. Chem. C*, 2018, **122**, 10999–11007.
43 M. Sliwa, S. Létard, I. Malfant, M. Nierlich, P. G. Lacroix, T. Asahi, H. Masuhara, P. Yu and K. Nakatani, *Chem. Mater.*, 2005, **17**, 4727–4735.
44 J. Quertinmont, L. Maschio, A. Datta and B. Champagne, *J. Phys. Chem. C*, 2020, **124**, 24451–24459.
45 E. O. Levina, I. Y. Chernyshov, A. P. Voronin, L. N. Alekseiko, A. I. Stash and M. V. Vener, *RSC Adv.*, 2019, **9**, 12520–12537.
46 V. R. Hathwar, T. S. Thakur, R. Dubey, M. S. Pavan, T. N. Guru Row and G. R. Desiraju, *J. Phys. Chem. A*, 2011, **115**, 12852–12863.
47 V. R. Thalladi, H.-C. Weiss, D. Bläser, R. Boese, A. Nangia and G. R. Desiraju, *J. Am. Chem. Soc.*, 1998, **120**, 8702–8710.
48 A. Sudheendranath, K. A. Sandeep, K. Avinash, P. Venugopalan, A. Kumar and S. P. Thomas, *Cryst. Growth Des.*, 2023, **23**, 4013–4024.
49 T. S. Thakur, M. T. Kirchner, D. Bläser, R. Boese and G. R. Desiraju, *CrystEngComm*, 2010, **12**, 2079–2085.
50 B. K. Saha, A. Saha and S. A. Rather, *Cryst. Growth Des.*, 2017, **17**, 2314–2318.
51 G. Cavallo, P. Metrangolo, R. Milani, T. Pilati, A. Priimagi, G. Resnati and G. Terraneo, *Chem. Rev.*, 2016, **116**, 2478–2601.
52 P. J. Costa, *Phys. Sci. Rev.*, 2019, **2**(111), 20170136.
53 P. Politzer, J. S. Murray, T. Clark and G. Resnati, *Phys. Chem. Chem. Phys.*, 2017, **19**, 32166–32178.
54 P. Metrangolo, F. Meyer, T. Pilati, G. Resnati and G. Terraneo, *Angew. Chem., Int. Ed.*, 2008, **47**, 6114–6127.
55 P. Metrangolo and G. Resnati, *Chem. – Eur. J.*, 2001, **7**, 2511–2519.
56 P. Metrangolo and G. Resnati, *IUCrJ*, 2014, **1**, 5–7.
57 G. R. Desiraju and R. Parthasarathy, *J. Am. Chem. Soc.*, 1989, **111**, 8725–8726.
58 H. Mutlu and L. Barner, *Macromol. Chem. Phys.*, 2022, **223**, 2200111.
59 R. Cernansky, *Nature*, 2015, **519**, 379–380.
60 G. M. Sheldrick, *Acta Crystallogr., Sect. A: Found. Adv.*, 2015, **71**, 3–8.
61 G. M. Sheldrick, *Acta Crystallogr., Sect. C: Struct. Chem.*, 2015, **71**, 3–8.
62 O. V. Dolomanov, L. J. Bourhis, R. J. Gildea, J. a. K. Howard and H. Puschmann, *J. Appl. Crystallogr.*, 2009, **42**, 339–341.
63 C. F. Macrae, I. Sovago, S. J. Cottrell, P. T. A. Galek, P. McCabe, E. Pidcock, M. Platings, G. P. Shields, J. S. Stevens, M. Towler and P. A. Wood, *J. Appl. Crystallogr.*, 2020, **53**, 226–235.
64 C. R. Groom, I. J. Bruno, M. P. Lightfoot and S. C. Ward, *Acta Crystallogr., Sect. B: Struct. Sci., Cryst. Eng. Mater.*, 2016, **72**, 171–179.
65 D. Braga, S. d'Agostino and F. Grepioni, *Organometallics*, 2012, **31**, 1688–1695.
66 M. Jabłoński, *Molecules*, 2021, **26**, 6319.
67 S. d'Agostino, F. Spinelli, E. Boanini, D. Braga and F. Grepioni, *Chem. Commun.*, 2016, **52**, 1899–1902.
68 T. Fujiwara, J. Harada and K. Ogawa, *J. Phys. Chem. B*, 2004, **108**, 4035–4038.
69 G. M. Mercier, K. Robeyns and T. Leyssens, *Cryst. Growth Des.*, 2016, **16**, 3198–3205.
70 R. Chatterjee, U. Chaudhari and S. Anand, *Adv. Funct. Mater.*, 2023, **33**, 2206301.
71 J. F. Reynes, V. Isoni and F. García, *Angew. Chem., Int. Ed.*, 2023, **62**, e202300819.